



Mesoscale modeling of electric double layer capacitors with three-dimensional ordered structures

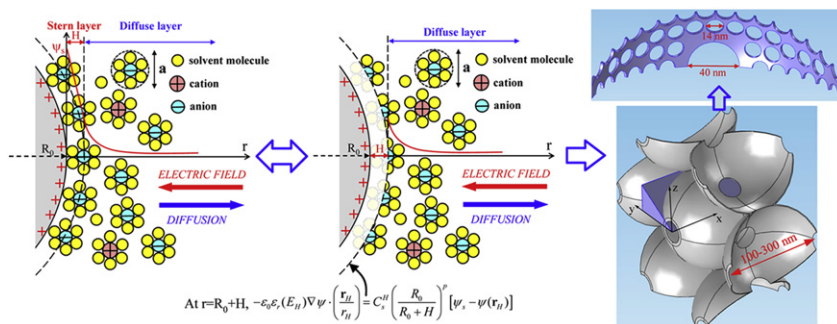
Hainan Wang¹, Laurent Pilon*

University of California, Los Angeles, Henry Samueli School of Engineering and Applied Science, Mechanical and Aerospace Engineering Department, 420 Westwood Plaza, Los Angeles, CA 90095, USA

HIGHLIGHTS

- New boundary conditions were derived to account for the Stern layer without simulating formally it.
- Both the Stern and diffuse layers were rigorously accounted for.
- The new boundary conditions were valid for planar, cylindrical, and spherical electrodes or pores.
- They made possible the simulations of EDLCs with highly ordered porous electrodes.
- Predictions of capacitances of an EDLC with ordered bimodal mesoporous carbons agreed well with experimental results.

GRAPHICAL ABSTRACT



ARTICLE INFO

Article history:

Received 14 March 2012

Received in revised form

3 July 2012

Accepted 1 August 2012

Available online 13 August 2012

Keywords:

Electric double layer

Electrochemical capacitors

Modified Poisson–Boltzmann model

Stern layer

Mesoscale modeling

Mesoporous electrodes

ABSTRACT

This paper presents general mathematical formulations for simulating electric double layer capacitors (EDLCs) with three-dimensional ordered structures. For the first time, a general set of boundary conditions was derived in order to account for the Stern layer without simulating it in the computational domain. These boundary conditions were valid for planar, cylindrical, and spherical electrode particles or pores. They made possible the simulations of EDLCs with complex geometries while rigorously accounting for both the Stern and diffuse layers. The model also simultaneously accounted not only for 3D electrode morphology but also for finite ion size and field-dependent electrolyte dielectric permittivity. It was used to faithfully simulate the complex structure of an EDLC electrode consisting of ordered bimodal mesoporous carbon featuring both macropores and mesopores. Areal and gravimetric capacitances were predicted based on non-solvated and solvated ion diameters. These two cases set the upper and lower bounds for the predicted capacitances. The capacitances predicted using non-solvated ion diameter were found to be in good agreement with experimental data reported in the literature. All surfaces contributed to the overall capacitance of EDLCs. The gravimetric capacitance of different bimodal carbons increased linearly with increasing specific surface area corresponding to constant areal capacitance.

© 2012 Elsevier B.V. All rights reserved.

1. Introduction

Electric double layer capacitors (EDLCs) have been the subject of intense studies in recent years due to their promises as electrical energy storage devices [1–5]. EDLCs store electric charges physically in the electric double layer forming at electrode/electrolyte

* Corresponding author. Tel.: +1 (310) 206 5598; fax: +1 (310) 206 2302.

E-mail address: pilon@seas.ucla.edu (L. Pilon).

¹ Tel.: +1 (310) 206 5598; fax: +1 (310) 206 2302.

interfaces accessible to ions present in the electrolyte [1–5]. Fig. 1(a) shows a schematic of the electric double layer structure forming near a positively charged cylindrical or spherical electrode particle. Solvated anions of diameter a migrate and adsorb to the electrode surface due to electrostatic forces while the cations are repelled [6–9]. The Stern layer is defined as the compact layer or inner layer near the electrode surface [6–9]. Note that there are no free charges within the Stern layer [6–8]. Beyond the Stern layer is the so-called diffuse layer where anions and cations are mobile under the coupled influence of electrostatic forces and diffusion [6–9].

Electrodes in EDLCs are typically made of mesoporous materials offering large surface area. Research efforts have focused on increasing the energy and power densities of supercapacitors by increasing the surface area of porous electrodes and tailoring their morphology or pore size distribution [1–5]. In particular, electrodes with three-dimensional ordered structures [10–27] have attracted significant attention due to [23–29] (1) their small ion transport

resistance, (2) their uniform pore connection leading to short ion diffusion length, and (3) their continuous electron transport framework. For example, Woo *et al.* [15] synthesized highly-ordered mesoporous carbon films as electrodes for EDLCs. These carbon films had ordered “bimodal” structure featuring both interconnected macropores and mesopores. In particular, their “CP204-S15” carbon film had specific surface area of $S_{BET} = 1003 \text{ m}^2 \text{ g}^{-1}$ [15]. The radius of the macropores and mesopores was reported to be 95 nm and 7 nm [15], respectively. The surface area due to micropores with diameter around or less than 2 nm was less than 6% [15]. From the FE-SEM image (Fig. 3(a) in Ref. [15]), the radius of the channels between macropores in “CP204-S15” carbon film was estimated to be 20 nm while the carbon wall thickness was about 2 nm. The electrolyte was 1 mol L⁻¹ (C₂H₅)₄NBF₄ (or TEABF₄) in propylene carbonate while the potential window was 2 V. The capacitances were measured using galvanostatic charge/discharge at low current density 40 mA g⁻¹ using the three-electrode method [15]. Finally, the areal and gravimetric capacitances for

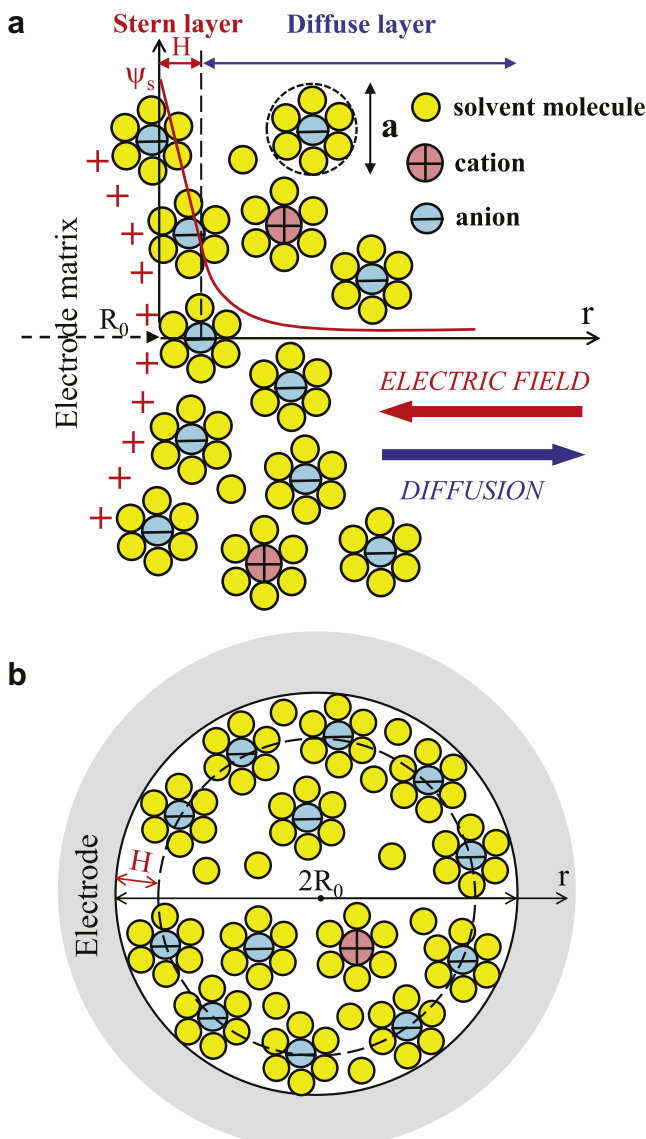


Fig. 1. Schematic of the electric double layer structure illustrating the arrangement of solvated anions and cations as well as the Stern and the diffuse layer forming near (a) a cylindrical or spherical electrode particle [6,7] and (b) a cylindrical or spherical pore with radius R_0 and Stern layer thickness H [6,7].

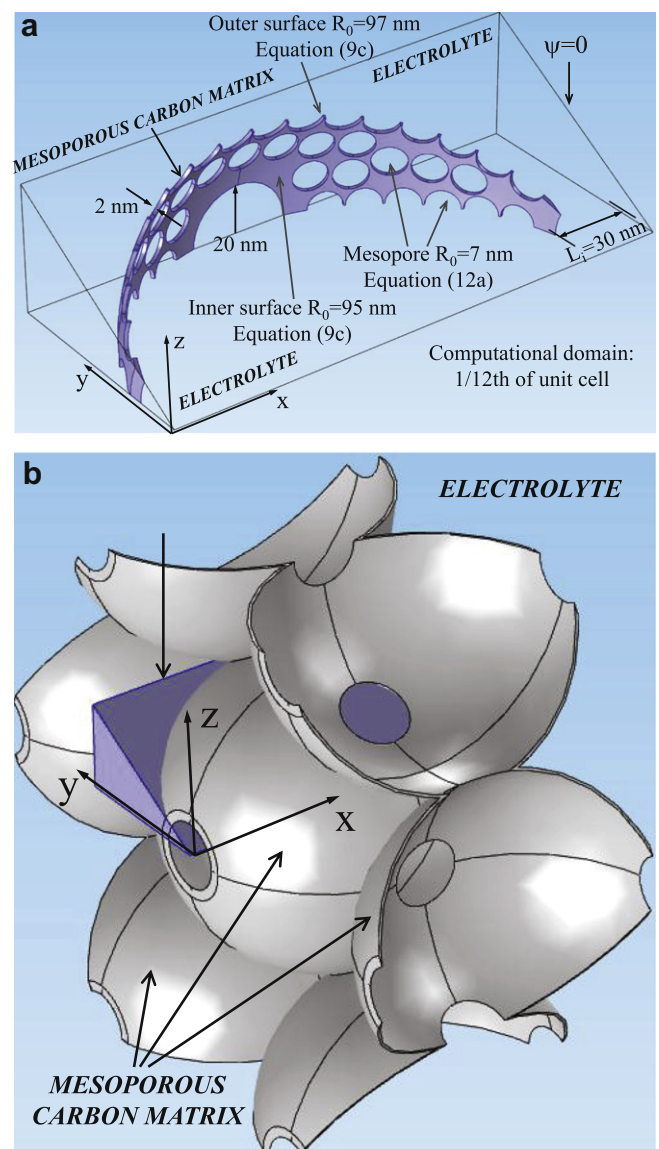


Fig. 2. Schematic and coordinate systems of (a) ordered bimodal carbon electrodes as synthesized in Ref. [15] and (b) the computational domain along with the boundary conditions and coordinate system for the ordered bimodal carbon CP204-S15 simulated in the present study.

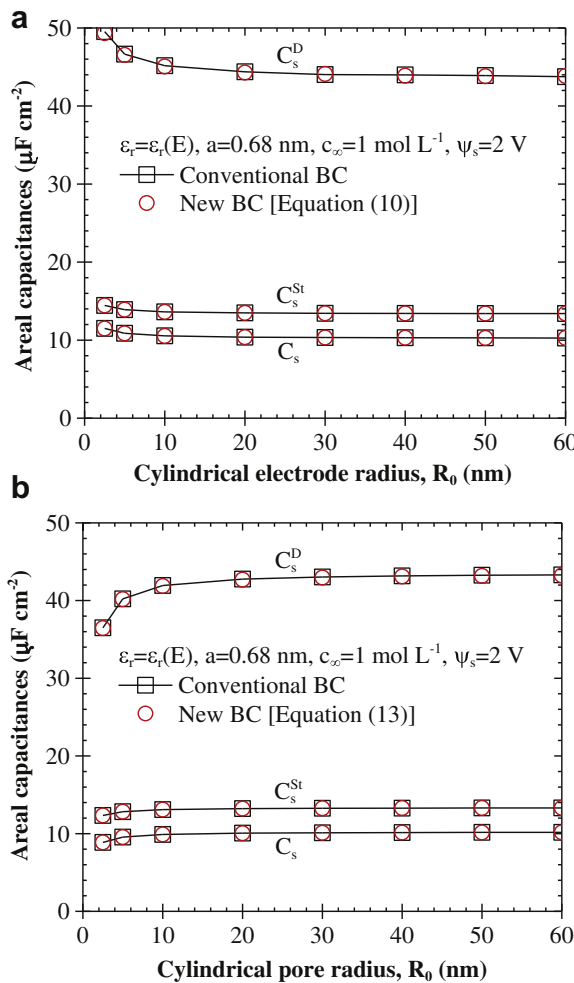


Fig. 3. Predicted Stern layer, diffuse layer, and total areal capacitances for (a) a cylindrical electrode particle and (b) a cylindrical pore as a function of radius R_0 ranging from 2.5 to 60 nm. Results were obtained using conventional and our new boundary conditions (BC) with $a = 0.68$ nm, $c_\infty = 1 \text{ mol L}^{-1}$, $\psi_s = 2 \text{ V}$, and electrolyte permittivity given by Equation (5).

the “CP204-S15” carbon film were reported to be $C_s = 9.4 \mu\text{F cm}^{-2}$ and $C_g = 95 \text{ F g}^{-1}$, respectively [15].

Numerous experimental studies have been devoted to characterizing the performances of EDLCs and assessing the effects of electrode morphology as well as of the physical or electrochemical properties of electrodes and electrolytes [1–5,10–27]. Experimental approaches are typically time consuming and costly. They also rely on trial and errors in order to optimize EDLCs. On the contrary, accurate and reliable numerical tools can facilitate the design and optimization of the electrode morphology in a more systematic and efficient way. Moreover, they can be used to understand the electrochemical and transport processes involved in EDLCs [30,31]. For example, they can predict the local electric potential and ion concentrations throughout the mesoporous electrodes [32–34] which cannot be measured experimentally. However, such numerical simulations are complicated by the multi-scales (from sub-nanometer to micron) and multi-physics nature of the problem. They should also be validated against experimental data.

This paper aims to develop a three-dimensional (3D) model based on continuum theory for simulating EDLCs with ordered mesoporous electrode structures. For the first time, the model simultaneously and rigorously accounts for (1) 3D electrode morphology, (2) finite ion size, (3) Stern and diffuse layers, and (4)

the dependency of the electrolyte dielectric permittivity on the local electric field. First, a new set of boundary conditions was derived to account for the Stern layer without simulating it in the electrolyte domain. The model was then used to simulate faithfully the electrode morphology of CP204-S15 mesoporous carbon EDLC synthesized and characterized by Woo *et al.* [15].

2. Background

2.1. Traditional modeling approaches

Equivalent RC circuit models and more complex transmission line models [35–37] have been traditionally used to simulate EDLCs. However, these models inherently neglect ion diffusion and non-uniform ion concentration in the electrolyte [30,31,38–40]. Thus, these models may not be valid for EDLCs under large electric potential and electrolyte concentration [30,31,38–41]. Alternatively, homogeneous models have also been developed to investigate the charging/discharging dynamics of EDLCs [42–47]. These models treat the heterogeneous microstructure of the electrodes as homogeneous with some effective macroscopic properties determined from effective medium approximations and depending on porosity and specific area [42–47]. In addition, they typically impose the areal capacitance or volumetric capacitance rather than predict them [42–47].

Moreover, the Helmholtz model [48–50] and Gouy–Chapman–Stern (GCS) model [51] are frequently used to simulate EDLCs with one- or two-dimensional electrode structure. In these models, the electrolyte dielectric permittivity is either assumed to be constant [50,51] or treated as a fitting parameter [48–50]. However, the relative permittivity ϵ_r of polar electrolytes is known to significantly decrease as the electric field increases [52–54]. In addition, the GCS model neglects the finite size of ions and treat ions as point-charges [32–34,55,56]. This assumption breaks down when either the electrolyte concentration c_∞ or the electric potential is large [30–34,55,56]. Therefore, the GCS model is invalid for practical EDLCs with typical electrolyte concentration larger than 1 mol L^{-1} and potential window larger than 1 V [34].

Due to their intrinsic limitations, none of the above-mentioned models can account for the three-dimensional mesoporous electrode morphology. The first equilibrium simulations of EDLCs with three-dimensional electrode morphology were reported by Pilon and co-workers [32,33]. These simulations also accounted for finite ion size as well as the dependency of the electrolyte dielectric permittivity on the local electric field [32,33]. However, the computations of the Stern and diffuse layer capacitances were decoupled due to the complex electrode structures [32,33]. Our recent study indicated that the Stern and diffuse layer need to be simulated simultaneously in order to predict accurately the electric double layer capacitances [34]. To the best of our knowledge, the Stern and diffuse layers have been simultaneously simulated only for one- or two-dimensional electrode structures such as planar electrodes [30,31] and a single cylindrical or spherical electrode particle or pore [34,48–51].

Under equilibrium conditions, the local electric potential $\psi(\mathbf{r})$ at location \mathbf{r} in the electrolyte can be found by solving the modified Poisson–Boltzmann (MPB) model with a Stern layer accounting for the finite ion size and expressed as [34,55,56],

$$\nabla \cdot (\epsilon_0 \epsilon_r \nabla \psi) = 0 \quad \text{in the Stern layer} \quad 1a$$

$$\nabla \cdot (\epsilon_0 \epsilon_r \nabla \psi) = \frac{2z_0 e N_A c_\infty \sinh\left(\frac{z_0 e \psi}{k_B T}\right)}{1 + 2\nu \sinh^2\left(\frac{z_0 e \psi}{2k_B T}\right)} \quad \text{in the diffuse layer} \quad 1b$$

Then, the local ion concentration $c(\mathbf{r})$ is given by [55,56]

$$c(\mathbf{r}) = \frac{c_\infty \exp(-z_0 e \psi / k_B T)}{1 + 2\nu \sinh^2\left(\frac{z_0 e \psi}{2k_B T}\right)} \quad (2)$$

where ϵ_0 and ϵ_r are the free space permittivity ($\epsilon_0 = 8.854 \times 10^{-12} \text{ F m}^{-1}$) and the relative permittivity of the electrolyte solution, respectively. The valency of the symmetric electrolyte is denoted by z_0 , while c_∞ is the bulk molar concentration of electrolyte, T is the absolute temperature, e is the elementary charge ($e = 1.602 \times 10^{-19} \text{ C}$), N_A and k_B are the Avogadro's number ($N_A = 6.022 \times 10^{23} \text{ mol}^{-1}$) and the Boltzmann constant ($k_B = 1.381 \times 10^{-23} \text{ m}^2 \text{ kg K}^{-1} \text{ s}^{-2}$), respectively. The packing parameter is defined as $\nu = 2a^3 N_A c_\infty$ where a is the effective ion diameter. It represents the ratio of the total bulk ion concentration to the maximum ion concentration $c_m = 1/N_A a^3$ assuming a simple cubic ion packing [40,55,56]. Therefore, ν should not be larger than unity for the model to be physically acceptable.

2.2. Conventional boundary conditions

Boundary conditions are required to predict the electric potential and ion concentration profile in the electrolyte. The electric potential at the electrode/electrolyte interface is typically prescribed under equilibrium conditions [6–9,32,34,56,57]. For a sphere or cylinder of radius R_0 , it is given by

$$\psi(r = R_0) = \psi_s, \quad (3a)$$

In addition, the electric potential and displacement are continuous across the Stern/diffuse layer interface located at $r = R_0 + H$ so that [6,30,31,58],

$$\begin{aligned} \psi(r = R_0 + H^-) &= \psi(r = R_0 + H^+) \quad \text{and} \\ \epsilon_0 \epsilon_r \frac{d\psi}{dr}(r = R_0 + H^-) &= \epsilon_0 \epsilon_r \frac{d\psi}{dr}(r = R_0 + H^+) \end{aligned} \quad (3b)$$

Far away from the electrode surface, the electric potential and ion concentration are constant such that [30–34,38],

$$\psi(r = R_0 + L_i) = 0 \quad \text{and} \quad c_i(r = R_0 + L_i) = c_\infty \quad (3c)$$

In fact, the presence of the very thin Stern layer near the electrode surface causes several numerical challenges. First, the Stern layer complicates the computational domain by introducing an additional length scale which is significantly smaller than that of the diffuse layer. Therefore, the computational domain becomes extremely complicated and the number of meshes prohibitively large for simulating three-dimensional electrode structures. Second, the governing equations for the electric potential and ion concentrations in the Stern and diffuse layers are numerically solved separately and coupled through the boundary conditions [Equation (3b)]. These equations must be solved simultaneously thus requiring excessive computational time and resources. Therefore, the MPB model with a Stern layer [Equation (1)] and the conventional boundary conditions [Equation (3)] [30,31,34,51] cannot be used to simulate three-dimensional structures such as those encountered in practical EDLCs.

Alternatively, the Stern layer forming near planar electrodes can also be accounted for via a modified boundary condition without simulating it explicitly in the electrolyte domain. In one-dimensional Cartesian coordinates, the corresponding boundary condition at the Stern/diffuse layer interface located at $x = H$ has been derived as [38,40,55,56,59–66],

$$\epsilon_0 \epsilon_r \frac{d\psi}{dx}(x = H) = C_s^{\text{St}} [\psi_s - \psi(x = H)] \quad (4)$$

where $C_s^{\text{St}} = \epsilon_0 \epsilon_r / H$ is the Stern layer capacitance for planar electrodes [38,40,55,56,59–66]. Then, Equations (3c) and (4) form a complete set of boundary conditions for the entire electric double layer while simulating only the diffuse layer from $x = H$ to $x = L_i$. To the best of our knowledge, no similar approach has been proposed for simulating electric double layers near electrodes in other geometries or coordinate systems.

This paper aims to develop a new set of boundary conditions to account for the Stern layer without simulating it in the computational domain for planar, cylindrical, and spherical electrode particles or pores. This presents the advantages of simplifying the computational domain by simulating only the diffuse layer and thus reducing the number of finite elements and the computational cost and time. Moreover, it also enables the simulations of three-dimensional highly-ordered mesoporous electrode structures. Finally, this approach was demonstrated and validated against experimental data for ordered bimodal carbon films reported in Ref. [15].

3. Analysis

3.1. Schematics and assumptions

Fig. 2(a) shows the schematic representation of the ordered bimodal mesoporous carbon simulated in this study. Here, the dimensions of the simulated electrode structure were identical to those of the bimodal mesoporous carbon "CP204-S15" reported in Ref. [15] as previously discussed. Note that the capacitances predicted by the MPB model with the Stern layer [Equation (1)] are identical for the positive and negative electrodes in binary and symmetric electrolytes [32,34,55,56] such as those considered here. Therefore, it suffices to simulate only one electrode [32,34,55,56]. In addition, the present study simulated one unit cell of the 3D porous electrode structure. Further increasing the number of unit cells was found to have no effect on the predicted areal and gravimetric capacitances under equilibrium conditions [32]. By virtue of symmetry, it suffices to simulate only 1/12th of one unit cell. Fig. 2(b) shows the schematic of the computational domain simulated in this study. The density of carbon materials is about $\rho = 1.8 \text{ g cm}^{-3}$ in its amorphous phase [67]. Then, the number of mesopores existing in the walls was adjusted so that the specific area of the simulated electrode matched that of the actual bimodal electrodes ranging from 492 to 1504 $\text{m}^2 \text{ g}^{-1}$ [15]. Overall, the specific area of the simulated structure [Fig. 2(b)] was adjusted to be 960 $\text{m}^2 \text{ g}^{-1}$ which falls within 5% of its experimental value of 1003 $\text{m}^2 \text{ g}^{-1}$ [15]. The thickness of the electrolyte region at the edge of the electrode was specified to be $L_i = 30 \text{ nm}$. Increasing this thickness to $L_i = 60 \text{ nm}$ was found to have no effect on the predicted areal and gravimetric capacitances due to the rapid decrease of the electric potential from the electrode surface caused by the thin electric double layer [32–34].

To make the problem mathematically tractable, the following assumptions were made: (1) the electric potential and ion concentrations reached their equilibrium states, (2) anions and cations had the same effective diameter assumed to be constant and independent of electrolyte concentration [55,56,68], (3) the electrolyte relative permittivity was constant and uniform within the Stern layer. Note that the electrolyte relative permittivity is typically defined for media with characteristic length larger than 1 or 2 nm [69,70], (4) isothermal conditions prevailed throughout the electrode and electrolyte, (5) advection of the electrolyte was assumed to be negligible, (6) the ions could only accumulate at the Stern/

diffuse layer interface and could not diffuse into the electrode, i.e., there was no ion insertion, and (7) the specific ion adsorption due to non-electrostatic forces were assumed to be negligible.

3.2. Constitutive relations

In order to solve Equations (1) and (3), the electrolyte properties ϵ_r , z_0 , c_∞ , and a along with the temperature T and the surface potential ψ_s are needed. In the diffuse layer, the Booth model was used to account for the dependency of electrolyte dielectric permittivity on the local electric field [32,34,52–54].

$$\epsilon_r(E) = n^2 + (\epsilon_r(0) - n^2) \frac{3}{\beta E} \left[\coth(\beta E) - \frac{1}{\beta E} \right] \quad \text{for } E \geq 10^7 \text{ V m}^{-1} \quad (5a)$$

$$\epsilon_r = \epsilon_r(0) \quad \text{for } E < 10^7 \text{ V m}^{-1} \quad (5b)$$

where $E = |\nabla\psi|$ is the norm of the local electrical field vector, $\epsilon_r(0)$ is the relative permittivity at zero electric field, and n is the index of refraction of the electrolyte at zero electric field frequency. In the Stern layer, the electrolyte dielectric permittivity was imposed as constant and uniform [assumption (3)]. Its value was evaluated using Equation (5) and the computed local electric field at the Stern/diffuse layer interface.

The electrolyte solution used in Ref. [15] was TEABF₄ in propylene carbonate solution at room temperature ($T = 298$ K) characterized by the following properties: $\epsilon_r(0) = 64.4$ [71], $n = 1.42$ [72], $\beta = 1.314 \times 10^{-8}$ m V⁻¹ [32], and $z_0 = 1$. The ion diameter of non-solvated TEA⁺ and BF₄⁻ ions are $a = 0.68$ and 0.34 nm [73], respectively. Their solvated ion diameters were reported to be $a = 1.36$ and 1.40 nm [74,75], respectively. The electrolyte concentration and the surface electric potential were chosen to be the same as those used in Ref. [15], namely, $c_\infty = 1.0$ mol L⁻¹ and $\psi_s = 2$ V. In addition, the Stern layer thickness H was approximated as the radius of solvated ions, i.e., $H = a/2$ [7–9].

3.3. Derivation of generalized boundary conditions

This section presents the derivation of a generalized boundary condition valid for cylindrical and spherical electrode particles or pores. For a cylindrical electrode of radius R_0 (Fig. 1(a)), Equation (1) in the Stern layer is expressed as [30,31,51]

$$\frac{d}{dr} \left(\epsilon_0 \epsilon_r r \frac{d\psi}{dr} \right) = 0 \quad \text{for } R_0 \leq r < R_0 + H \quad (6)$$

where $\epsilon_r = \epsilon_r(E_H)$ is the uniform electrolyte relative permittivity within the Stern layer [assumption (3)]. Its value is evaluated at the Stern/diffuse layer interface located at $r_H = R_0 + H$ using Booth model [Equation (5)] based on the local electric field $E_H(r_H)$. Then, integrating Equation (6) twice with respect to r from $r = R_0$ to $r = R_0 + H$ using the boundary condition given by Equations (3a) and (3b) yields,

$$\psi(r) = -[\psi_s - \psi(r = R_0 + H)] \frac{\log(r/R_0)}{\log(1 + H/R_0)} + \psi_s \quad (7)$$

Differentiation of Equation (7) with respect to r yields the following boundary condition at the Stern/diffuse layer interface at $r = R_0 + H$,

$$-\epsilon_0 \epsilon_r(E_H) \frac{d\psi}{dr}(r = R_0 + H) = \frac{\epsilon_0 \epsilon_r(E_H)}{R_0 \log(1 + H/R_0)} \frac{R_0}{R_0 + H} \times [\psi_s - \psi(r = R_0 + H)] \quad (8)$$

Equation (8) relates the local electric potential to its gradient at $r = R_0 + H$. It serves as a new boundary condition at the Stern/diffuse layer interface.

Similarly, for spherical electrodes, the boundary condition at the Stern/diffuse layer interface can be derived as,

$$-\epsilon_0 \epsilon_r(E_H) \frac{d\psi}{dr}(r = R_0 + H) = \frac{\epsilon_0 \epsilon_r(E_H)}{H} \left(1 + \frac{H}{R_0} \right) \left(\frac{R_0}{R_0 + H} \right)^2 \times [\psi_s - \psi(r = R_0 + H)] \quad (9)$$

Note that Equations (4), (8) and (9) can be rewritten in a generalized form for planar, cylindrical, and spherical electrodes as,

$$-\epsilon_0 \epsilon_r(E_H) \nabla \psi \cdot \left(\frac{\mathbf{r}_H}{r_H} \right) = C_s^H \left(\frac{R_0}{R_0 + H} \right)^p [\psi_s - \psi(r_H)] \quad (10)$$

where \mathbf{r}_H is the local position vector at the Stern/diffuse layer interface located at $r_H = R_0 + H$ for cylindrical and spherical electrodes. Note that \mathbf{r}_H/r_H represents the local outward normal unit vector at the Stern/diffuse layer interface. Here, C_s^H is the Stern layer capacitance predicted by the Helmholtz model assuming constant ϵ_r within the Stern layer and given by [34,76],

$$C_s^H = \frac{\epsilon_0 \epsilon_r(E_H)}{H} \quad \text{for planar electrode} \quad 11a$$

$$C_s^H = \frac{\epsilon_0 \epsilon_r(E_H)}{R_0 \log(1 + H/R_0)} \quad \text{for cylindrical electrode} \quad 11b$$

$$C_s^H = \frac{\epsilon_0 \epsilon_r(E_H)}{H} \left(1 + \frac{H}{R_0} \right) \quad \text{for spherical electrode} \quad 11c$$

The value of p in Equation (10) is given by,

$$p = 0 \quad \text{for planar electrodes} \quad 12a$$

$$p = 1 \quad \text{for cylindrical electrodes} \quad 12b$$

$$p = 2 \quad \text{for spherical electrodes} \quad 12c$$

Moreover, for cylindrical and spherical pores of radius R_0 illustrated in Fig. 1(b), the new boundary condition at the Stern/diffuse layer interface located at $r_H = R_0 - H$ can be similarly derived as,

$$-\epsilon_0 \epsilon_r(E_H) \nabla \psi \cdot \left(\frac{\mathbf{r}_H}{r_H} \right) = C_s^H \left(\frac{R_0}{R_0 - H} \right)^p [\psi_s - \psi(r_H)] \quad (13)$$

where $p = 1$ or 2 for cylindrical or spherical pores, respectively. Here also, the Stern layer capacitance C_s^H for cylindrical or spherical pores is given by the Helmholtz model assuming constant ϵ_r within the Stern layer and expressed as [76],

$$C_s^H = \frac{\epsilon_0 \epsilon_r(E_H)}{R_0 \log\left(\frac{R_0}{R_0 - H}\right)} \quad \text{for cylindrical pores of radius } R_0 \quad 14a$$

$$C_s^H = \frac{\epsilon_0 \epsilon_r(E_H)}{H} \left(\frac{R_0 - H}{R_0} \right) \quad \text{for spherical pores of radius } R_0 \quad 14b$$

3.4. Method of solution and data processing

Equation (1) was solved using the commercial finite element solver COMSOL 4.2, along with the boundary conditions given by Equations (3c) and (10) or (13) and field-dependent permittivity $\epsilon_r(E)$ given by Equation (5). The simulations were run on a Dell

workstation Precision 690 with two 2.66 GHz Quad-Core Intel Xeon CPUs and 64 GB of RAMs.

Due to charge conservation [Equation (1)], the total amount of charges Q stored near the electrode surfaces A_s is equal to that present at the Stern/diffuse layer interface denoted by A_d . Then, it can be computed by integrating the surface charge density ($\epsilon_0 \epsilon_r \mathbf{E} \cdot \mathbf{n}$) along A_s or A_d and expressed as [8,77],

$$Q = \int_{A_s} \epsilon_0 \epsilon_r(E) \mathbf{E} \cdot \mathbf{n} \, dA = \int_{A_d} \epsilon_0 \epsilon_r(E) \mathbf{E} \cdot \mathbf{n} \, dA \quad (15)$$

where $\mathbf{E} = -\nabla\psi$ is the local electric field vector, \mathbf{n} is the local outward normal unit vector at the electrode surface A_s or at the electrode/electrolyte interface A_d . Then, the overall gravimetric capacitance was estimated as [33],

$$C_g = \frac{Q}{\rho V \psi_s} \quad (16)$$

where ρ and V are the density and volume of the amorphous carbon electrode, respectively. The diffuse layer areal capacitance C_s^D and the total areal capacitance C_s were respectively estimated as [32,33],

$$C_s^D = \frac{Q}{\psi_d A_d} = \frac{1}{\psi_d A_d} \int_{A_d} \epsilon_0 \epsilon_r(E) \mathbf{E} \cdot \mathbf{n} \, dA \quad \text{and} \quad C_s = \frac{Q}{\psi_s A_s} \quad (17)$$

Note that the total areal capacitance C_s can be also equivalently calculated using the one-dimensional series formula $1/C_s = 1/C_s^{\text{St}} + 1/C_s^D$ when the Stern layer thickness is much smaller than the electrode or pore diameter as considered here. In addition, the Stern layer areal capacitance C_s^{St} was given by the Helmholtz model [Equation (11) or Equation (14)].

The numerical convergence criterion was defined such that the maximum relative differences in the predicted capacitances C_s^{St} , C_s^D , C_s , and C_g was less than 1.5% when decreasing the mesh size by a factor two. The mesh size was the smallest at the Stern/diffuse layer interface due to the large electric potential gradient and then gradually increased. The maximum mesh size was specified to be about 0.1 nm at all Stern/diffuse layer interfaces and remained less than 2.5 nm anywhere else in the computational domain. The total number of finite elements was on the order of 10^7 for the simulations of bimodal ordered carbon CP204-S15 with 1/12th of one unit cell shown in Fig. 2(b).

Finally, the numerical tool was validated based on two equilibrium cases reported in the literature. First, the equilibrium electric potential profile in the diffuse layer predicted by solving the MPB model was validated against the exact solution for planar electrodes [6,8,58] with $\epsilon_r = 78.5$, $c_\infty = 0.01$ and 0.001 mol L^{-1} , $\nu = 0$, and $\psi_D = 0.1 \text{ V}$. Second, the computed capacitances for the Stern and diffuse layers obtained from the MPB model were validated against their theoretical formula assuming constant electrolyte permittivity [34,55,56] for $\psi_s = 2 \text{ V}$, $c_\infty = 1 \text{ mol L}^{-1}$, and $a = 0.68$ or 1.40 nm . Good agreement was obtained between our results and reported electric potential profiles [6,8,58] or capacitances [34,55,56] for all cases considered.

4. Results and discussions

4.1. Validity of the new boundary conditions

The new boundary conditions [Equations (10) and (13)] were used to compute the capacitances for a single cylindrical electrode particle and a cylindrical pore by solving Equations (1b), (3c) and (10) or Equation (13), respectively. The parameters were chosen

such that $a = 0.68 \text{ nm}$, $c_\infty = 1.0 \text{ mol L}^{-1}$, and $\psi_s = 2 \text{ V}$ with field-dependent electrolyte permittivity $\epsilon_r(E)$ given by Equation (5). The results were compared with those obtained by simulating both the Stern and diffuse layers in the electrolyte domain using the conventional boundary conditions given by Equation (3). Fig. 3 shows the Stern layer, diffuse layer, and total areal capacitances predicted using these two approaches as a function of particle or pore radius R_0 ranging from 2.5 to 60 nm. The relative difference in the values of C_s^{St} , C_s^D , and C_s predicted using these two approaches was less than 0.2% for all cases considered here. In addition, it is evident that the predicted C_s^{St} was much smaller than C_s^D for all cases considered. Therefore, the double layer capacitance C_s was dominated by C_s^{St} which is consistent with the conclusion drawn in our previous study [34] when accounting for field-dependent electrolyte permittivity. Note that for particle or pore radius larger than 40 nm, the predicted capacitance reached a plateau of $C_s = 10.2 \mu\text{F cm}^{-2}$ corresponding to that of planar electrodes as discussed in Refs. [32–34,49,50].

Similarly, the predicted capacitances C_s^{St} , C_s^D , and C_s using these two approaches were compared for a spherical electrode and a spherical pore with various radii ranging from 2.5 to 60 nm. Excellent agreement was observed in all cases. Overall, these results demonstrate that the Stern layer can be accurately accounted for by using the new boundary conditions given by Equation (10) or Equation (13) for cylindrical and spherical electrodes or pores without explicitly simulating the Stern layer in the electrolyte domain. Note that the total number of finite elements decreased by about 30%–60% when using the new boundary conditions for simulating a single cylindrical and spherical electrode or pore with radius ranging from 2.5 to 60 nm. The corresponding computational time was reduced by about 10%–30%. This reduction in finite elements and computational time became more significant with increasing radius and geometric complexity. This clearly demonstrates the advantage of the new boundary conditions.

4.2. Capacitances of ordered bimodal carbons

The double layer capacitances C_s^{St} , C_s^D , and C_s of the ordered bimodal carbon shown in Fig. 2(b) were predicted by solving Equation (1b) in the diffuse layer along with the new boundary conditions given by Equations (3c) and (10) or Equation (13). The electrode surface was divided in three sections (i) the inner surface of the pores of radius 95 nm, (ii) the outer surface of radius 97 nm, and (iii) the mesopore with 7 nm in radius located in the walls separating the macropores. The boundary condition given by Equation (10) was imposed at the outer surfaces while Equation (13) was imposed at the mesopore and inner pore surfaces, respectively. Note that without these new boundary conditions, it was impossible to solve the coupled governing equations for such a complex domain due to (i) the difficulty in creating the geometry and (ii) an excessively large number of finite elements.

Table 1 summarizes the predicted Stern layer, diffuse layer, and total areal capacitances as well as the gravimetric capacitance at the inner, outer, and mesopore surfaces of the ordered bimodal carbon. Results were obtained based on the non-solvated effective ion diameter $a = 0.68 \text{ nm}$ [73] with field-dependent electrolyte permittivity $\epsilon_r(E)$ given by Equation (5). The areal capacitances predicted for planar electrodes for the same parameters were also reported in Table 1 for comparison purposes.

It is evident that the Stern layer areal capacitance C_s^{St} was about one-third smaller than the diffuse layer areal capacitance C_s^D at all surfaces. Thus, the total areal capacitance C_s was controlled by the Stern layer. In addition, the total areal capacitances C_s at the inner and outer surfaces were $10.2 \mu\text{F cm}^{-2}$ which was identical to that

Table 1

Predicted Stern layer C_s^{St} , diffuse layer C_s^D , and total C_s areal capacitances as well as gravimetric capacitance for the ordered bimodal carbon (Fig. 2(b)) computed at the inner, outer, and mesopore surfaces. Results were obtained by solving Equations (1b), (3c) and (10) or Equation (13) using non-solvated or solvated ion diameter $a = 0.68$ or $a = 1.40$ nm, respectively along with $c_m = 1 \text{ mol L}^{-1}$, $\psi_s = 2 \text{ V}$, and electrolyte permittivity given by Equation (5). Predictions for planar electrodes are reported for comparison.

Ion diameter	Capacitance	Planar electrode	Inner surface	Outer surface	Mesopores
$a = 0.68 \text{ nm}$	$C_s^{\text{St}} (\mu\text{F cm}^{-2})$	13.4	13.3	13.4	12.8
	$C_s^D (\mu\text{F cm}^{-2})$	43.2	44.6	43.8	47.3
	$C_s (\mu\text{F cm}^{-2})$	10.2	10.2	10.2	10.1
	$C_g (\text{F g}^{-1})$	—	39.0	35.0	23.0
	$C_s^{\text{St}} (\mu\text{F cm}^{-2})$	13.0	11.8	11.9	10.0
	$C_s^D (\mu\text{F cm}^{-2})$	17.7	21.4	20.7	28.5
$a = 1.40 \text{ nm}$	$C_s (\mu\text{F cm}^{-2})$	7.5	7.5	7.5	7.4
	$C_g (\text{F g}^{-1})$	—	29.2	25.1	17.8

for planar electrodes. Indeed, electrodes with radius of curvature larger than 40 nm behave like planar electrodes as established in Refs. [32,34] and also shown in Fig. 3. Similarly, the areal capacitance C_s at mesopore surfaces was $10.1 \mu\text{F cm}^{-2}$ which fell within 1% of that of planar electrodes. In fact, it was found that the areal capacitance C_s of mesopores decreased with increasing pore depth (or carbon wall thickness) (not shown). This was due to the confinement of the electric field in small pores leading to reduced surface charge density and capacitance as previously discussed [32,33]. However, this effect appeared to be negligible for small pore depth (i.e., carbon wall thickness) of 2 nm such as those considered here. In addition, the mesopores contributed about 30% less to the gravimetric capacitance C_g than the inner and outer pore surfaces. This was due to the small carbon wall thickness and thus the relatively small mesopore surface area compared with those of inner and outer pore surfaces.

Table 1 also summarizes the predicted capacitances for the electrode structure shown in Fig. 2(b) but using solvated ion diameter $a = 1.40 \text{ nm}$ [75]. It demonstrates that, for larger effective ion diameter, the Stern layer areal capacitance C_s^{St} had the same order of magnitude as the diffuse layer areal capacitance C_s^D at all surfaces. Consequently, the capacitances C_s^{St} and C_s^D contributed nearly equally to the total areal capacitance C_s . Here also, the inner and outer pore surfaces contributed slightly more to the gravimetric capacitance than mesopores. However, both the local areal and gravimetric capacitances decreased by about 30% when using the solvated ion diameter $a = 1.40 \text{ nm}$ instead of $a = 0.68 \text{ nm}$. This was due to the associated reduction in the maximum ion concentration $c_m = 1/N_A a^3$ at the electrode surface as ion diameter a increases.

Finally, for the relatively large surface potential $\psi_s = 2 \text{ V}$ considered, the ion concentration given by Equation (2) reached its maximum value c_m at all surfaces in the simulations (not shown) regardless of the value chosen for the effective ion diameter a .

4.3. Comparison with experimental data

Table 2 shows the predicted overall areal and gravimetric capacitances C_s and C_g defined by Equations (16) and (17) and accounting for the contribution of all electrode surfaces. The experimental values reported in Ref. [15] are also reproduced for comparison. It is worth noting that the values of C_s and C_g predicted using non-solvated ion diameter $a = 0.68 \text{ nm}$ were about 8.5% and 3% larger than their respective experimental counterparts. On the other hand, C_s and C_g predicted using solvated ion diameter $a = 1.40 \text{ nm}$ underestimated the experimental values by about 24%. In fact, the predictions using non-solvated and solvated ion

Table 2

Predicted overall areal and gravimetric capacitances of the ordered bimodal carbon using (a) non-solvated ion diameter $a = 0.68 \text{ nm}$ and (b) solvated ion diameter $a = 1.40 \text{ nm}$ in comparison with experimental data reported in Ref. [15]. Results were obtained by solving Equations (3c), (1b) and (10) or Equation (13) with $c_\infty = 1 \text{ mol L}^{-1}$ and $\psi_s = 2 \text{ V}$.

	Specific area ($\text{m}^2 \text{ g}^{-1}$)	$C_s (\mu\text{F cm}^{-2})$	$C_g (\text{F g}^{-1})$
Measured [15]	1003	9.4	95
$a = 0.68 \text{ nm}$	960	10.2	97.9
$a = 1.40 \text{ nm}$	960	7.5	72.0

diameters set the upper and lower bounds for the capacitances, respectively. The capacitances predicted using non-solvated ion diameter ($a = 0.68 \text{ nm}$ [73]) showed better agreement with experimental data. We speculate that these results could be attributed to two possible reasons. First, as the electrolyte concentration increases, the dissolved electrolyte ions become less solvated, i.e., they are surrounded by less solvent molecules [16,78–80]. Consequently, the effective ion diameter decreases with increasing electrolyte concentration [16,78,79]. Note also that the solubility of TEABF₄ in propylene carbonate is about 1 mol L^{-1} at room temperature [81]. Second, the effective ion diameter of TEA⁺ tends to decrease under large local electric field [82]. In fact, TEA⁺ ions was found to become distorted and able to adsorb in pores with diameter even smaller than the non-solvated TEA⁺ [82–84]. Thus, the effective ion diameter near the electrode surfaces approaches that of the non-solvated ions, i.e., $a = 0.68 \text{ nm}$ [82–84]. Overall, the predicted capacitances agreed well with experimental data. These results validate the numerical models, boundary conditions, and constitutive relationships developed here for simulating EDLCs with three-dimensional ordered structures. The new boundary conditions were essential in obtaining such results.

Thanks to this experimentally validated numerical model, it becomes possible to numerically explore the effects of the electrode architecture on its energy storage capabilities. Fig. 4 shows the predicted gravimetric capacitance C_g of bimodal carbon structures as a function of their specific surface area ranging from 910 to 1030 $\text{m}^2 \text{ g}^{-1}$. Here, the specific surface area was varied by changing the inner pore radius R_0 from 50 to 150 nm while other geometric parameters such as the carbon wall thickness and mesopore radius remained identical to those of CP204-S15 carbon shown in Fig. 2(b).

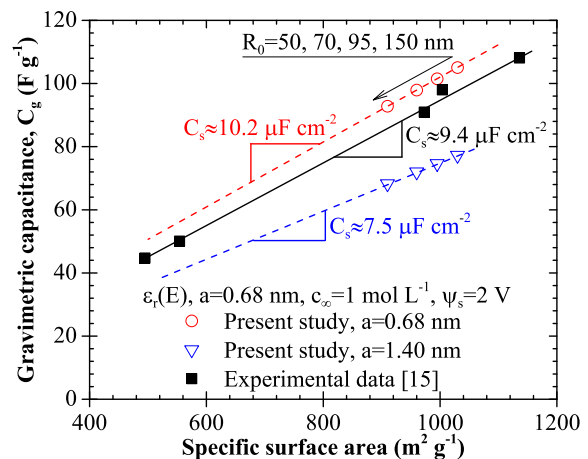


Fig. 4. Predicted and experimentally measured [15] gravimetric capacitance C_g for bimodal carbons as a function of their specific surface area. Numerical results were obtained by solving Equation (1b) using boundary conditions given by Equations (3c) and (10) or Equation (13) with non-solvated ion diameter $a = 0.68 \text{ nm}$, $c_\infty = 1 \text{ mol L}^{-1}$, $\psi_s = 2 \text{ V}$, and the electrolyte permittivity given by Equation (5). The inner pore radius R_0 was varied from 50 to 150 nm.

The results were obtained by solving Equation (1b) subject to boundary conditions given by Equations (3c) and (10) or Equation (13) using both solvated and non-solvated ion diameters, i.e., $a = 1.40$ nm and $a = 0.68$ nm, respectively. Other parameters were identical to those used to generate the results presented in Table 1. Fig. 4 also shows the measured gravimetric capacitance of different bimodal carbon films [15] obtained using 1 mol L⁻¹ TEABF₄ electrolyte. It is evident that predicted and experimentally measured gravimetric capacitance C_g increased linearly with increasing specific surface area. The slope of C_g vs. specific surface area corresponds to a constant areal capacitance of $C_s \approx 7.4$ or 10.2 $\mu\text{F cm}^{-2}$ when using solvated or non-solvated ion diameter, respectively. Note that this trend is consistent with experimental data reporting a linear relationship between gravimetric capacitance and specific surface area with an areal capacitance of 9.4 $\mu\text{F cm}^{-2}$ [15]. Overall, very good agreement was observed between experimental measurements and model predictions.

Finally, it is evident that the new boundary conditions [Equations (10) and (13)] developed here made possible the simulations of EDLCs with three-dimensional ordered electrode structures. These simulations can give detailed information such as the local charge storage, electric potential, and ion concentrations within the electrolyte which cannot be measured experimentally. Note also that these boundary conditions [Equations (10) and (13)] can be readily employed to simulate the dynamic charging and discharging of EDLCs with ordered electrode structures. Then, the model could be used to identify the optimum electrode architecture and provide design rules to achieve maximum charging performance by EDLCs.

5. Conclusion

This paper developed a three-dimensional (3D) model based on continuum theory for simulating EDLCs with ordered electrode structures. For the first time, a new set of boundary conditions was derived to account for the Stern layer forming near planar, cylindrical, and spherical electrodes as well as cylindrical and spherical pores. They made possible the simulations of EDLCs with 3D ordered electrode structures while simultaneously and accurately accounting for (i) both the Stern and diffuse layers, (ii) finite ion size, and (iii) the dependency of electrolyte permittivity on the local electric field. The model was used to faithfully simulate an actual EDLC consisting of complex 3D ordered bimodal carbons in 1 mol L⁻¹ TEABF₄/propylene carbonate electrolyte solution [15]. The predicted gravimetric capacitance of different bimodal carbons was found to increase linearly with increasing specific surface area corresponding to constant areal capacitance. Numerical predictions were in very good agreement with experimental data [15].

Acknowledgment

This material is based upon work supported as part of the Molecularly Engineered Energy Materials, an Energy Frontier Research Center funded by the U.S. Department of Energy, Office of Science, Office of Basic Energy Sciences under Award Number DE-SC0001342.

References

- [1] D. Pech, M. Brunet, H. Durou, P. Huang, V. Mochalin, Y. Gogotsi, P.L. Taberna, P. Simon, *Nature Nanotechnology* 5 (9) (2010) 651–654.
- [2] A.G. Pandolfo, A.F. Hollenkamp, *Journal of Power Sources* 157 (1) (2006) 11–27.
- [3] E. Frackowiak, *Physical Chemistry Chemical Physics* 9 (15) (2007) 1774–1785.
- [4] P. Simon, Y. Gogotsi, *Nature Materials* 7 (11) (2008) 845–854.
- [5] L.L. Zhang, X.S. Zhao, *Chemical Society Reviews* 38 (9) (2009) 2520–2531.
- [6] R.J. Hunter, *Foundations of Colloid Science*, second ed., Oxford University Press, Oxford, UK, 2001.
- [7] A.J. Bard, L.R. Faulkner, *Electrochemical Methods: Fundamentals and Applications*, John Wiley & Sons, New York, NY, 2001.
- [8] J.H. Masliyah, S. Bhattacharjee, *Electrokinetic and Colloid Transport Phenomena*, John Wiley & Sons, Hoboken, NJ, 2006.
- [9] H.J. Butt, M. Kappl, *Surface and Interfacial Forces*, Wiley-VCH Verlag GmbH & Co. KGaA, Weinheim, Germany, 2010.
- [10] J. Lee, S. Yoon, T. Hyeon, S.M. Oh, K.B. Kim, *Chemical Communications* 21 (1999) 2177–2178.
- [11] H. Zhou, S. Zhu, M. Hibino, I. Honma, *Journal of Power Sources* 122 (2) (2003) 219–223.
- [12] C. Vix-Guterl, E. Frackowiak, K. Jurewicz, M. Fribe, J. Parmentier, F. Beguin, *Carbon* 43 (6) (2005) 1293–1302.
- [13] D.W. Wang, F. Li, H.T. Fang, M. Liu, G.Q. Lu, H.M. Cheng, *Journal of Physical Chemistry B* 110 (17) (2006) 8570–8575.
- [14] H. Yamada, H. Nakamur, F. Nakahara, I. Moriguchi, T. Kudo, *Journal of Physical Chemistry C* 111 (1) (2007) 227–233.
- [15] S.W. Woo, K. Dokko, H. Nakano, K. Kanamura, *Journal of Materials Chemistry* 18 (14) (2008) 1674–1680.
- [16] H.J. Liu, W.J. Cui, L.H. Jin, C.X. Wang, Y.Y. Xia, *Journal of Materials Chemistry* 19 (22) (2009) 3661–3667.
- [17] H.J. Liu, X.M. Wang, W.J. Cui, Y.Q. Dou, D.Y. Zhao, Y.Y. Xia, *Journal of Materials Chemistry* 20 (20) (2010) 4223–4230.
- [18] G. Sun, J. Wang, X. Liu, D. Long, W. Qiao, L. Ling, *Journal of Physical Chemistry C* 114 (43) (2010) 18745–18751.
- [19] Y. Korenblit, M. Rose, E. Kockrick, L. Borchardt, A. Kvist, S. Kaskel, G. Yushin, *ACS Nano* 4 (3) (2010) 1337–1344.
- [20] D. Feng, Y. Lv, Z. Wu, Y. Dou, L. Han, Z. Sun, Y. Xia, G. Zheng, D. Zhao, *Journal of the American Chemical Society* 133 (38) (2011) 15148–15156.
- [21] N. Liu, H. Song, X. Chen, *Journal of Materials Chemistry* 21 (14) (2011) 5345–5351.
- [22] J. Wang, C. Xue, Y. Lv, F. Zhang, B. Tu, D. Zhao, *Carbon* 49 (13) (2011) 4580–4588.
- [23] J.-W. Lang, X.-B. Yan, X.-Y. Yuan, J. Yang, Q.-J. Xue, *Journal of Power Sources* 196 (23) (2011) 10472–10478.
- [24] W. Xing, S.Z. Qiao, R.G. Ding, F. Lid, G.Q. Lu, Z.F. Yan, H.M. Cheng, *Carbon* 44 (2) (2006) 216–224.
- [25] H.Q. Li, R.L. Liu, D.Y. Zhao, Y.Y. Xia, *Carbon* 45 (13) (2007) 2628–2635.
- [26] H.Q. Li, J.Y. Luo, X.F. Zhou, C.Z. Yu, Y.Y. Xia, *Journal of the Electrochemical Society* 154 (8) (2007) 731–736.
- [27] C. Liang, Z. Li, S. Dai, *Angewandte Chemie International Edition* 47 (20) (2008) 3696–3717.
- [28] C. Liu, F. Li, L.P. Ma, H.M. Cheng, *Advanced Materials* 22 (8) (2010) 28–62.
- [29] Y. Deng, Y. Cai, Z. Sun, D. Gu, J. Wei, W. Li, X. Guo, J. Yang, D. Zhao, *Advanced Functional Materials* 20 (21) (2010) 3658–3665.
- [30] H. Wang, L. Pilon, *Electrochimica Acta* 63 (2012) 55–63.
- [31] H. Wang, L. Pilon, *Electrochimica Acta* 64 (2012) 130–139.
- [32] H. Wang, J. Varghese, L. Pilon, *Electrochimica Acta* 56 (17) (2011) 6189–6197.
- [33] J. Varghese, H. Wang, L. Pilon, *Journal of the Electrochemical Society* 158 (10) (2011) 1106–1114.
- [34] H. Wang, L. Pilon, *Journal of Physical Chemistry C* 115 (33) (2011) 16711–16719.
- [35] W.G. Pell, B.E. Conway, *Journal of Electroanalytical Chemistry* 500 (1–2) (2001) 121–133.
- [36] W.G. Pell, B.E. Conway, *Journal of Power Sources* 96 (1) (2001) 57–67.
- [37] W. Lajnef, J.M. Vinassa, O. Briat, S. Azzopardi, E. Woirgard, *Journal of Power Sources* 168 (2) (2007) 553–560.
- [38] M.Z. Bazant, K. Thornton, A. Ajdari, No. 021506, *Physical Review E* 70 (2) (2004) 1–24.
- [39] K.T. Chu, M.Z. Bazant, No. 011501, *Physical Review E* 74 (1) (2006) 1–25.
- [40] L.H. Olesen, M.Z. Bazant, H. Bruus, No. 011501, *Physical Review E* 82 (1) (2010) 1–29.
- [41] E.J.F. Dickinson, R.G. Compton, *Journal of Electroanalytical Chemistry* 655 (1) (2011) 23–31.
- [42] A.M. Johnson, J. Newman, *Journal of the Electrochemical Society* 118 (3) (1971) 510–517.
- [43] B. Pillay, *Design of Electrochemical Capacitors for Energy Storage*. Ph.D Thesis, Department of Chemical Engineering, University of California, Berkeley, CA, 1996.
- [44] V. Srinivasan, J.W. Weidner, *Journal of the Electrochemical Society* 146 (5) (1999) 1650–1658.
- [45] M.W. Verbrugge, P. Liu, *Journal of the Electrochemical Society* 152 (5) (2005) 79–87.
- [46] S. Kazaryan, S. Razumov, S. Litvinenko, G. Kharisov, V. Kogan, *Journal of the Electrochemical Society* 153 (9) (2006) 1655–1671.
- [47] S.K. Griffiths, R.H. Nilson, *Journal of the Electrochemical Society* 157 (4) (2010) 469–479.
- [48] J. Huang, B.G. Sumpter, V. Meunier, *Angewandte Chemie International Edition* 47 (3) (2008) 520–524.
- [49] J. Huang, B.G. Sumpter, V. Meunier, *Chemistry—A European Journal* 14 (22) (2008) 6614–6626.
- [50] J. Huang, B.G. Sumpter, V. Meunier, G. Yushin, C. Portet, Y. Gogotsi, *Journal of Materials Research* 25 (8) (2010) 1525–1531.

- [51] J. Huang, R. Qiao, B.G. Sumpter, V. Meunier, *Journal of Materials Research* 25 (8) (2010) 1469–1475.
- [52] F. Booth, *Journal of Chemical Physics* 19 (4) (1951) 391–394.
- [53] F. Booth, *Journal of Chemical Physics* 23 (3) (1955) 453–457.
- [54] A.J. Appleby, in: B. Conway, C. Vayenas, R. White, M. Gamboa-Adelco (Eds.), *Modern Aspects of Electrochemistry*, Kluwer Academic/Plenum Publishers, New York, NY, 2005, pp. 175–301.
- [55] M.S. Kilic, M.Z. Bazant, A. Ajdari, *Physical Review E* 75 (2) (2007) 1–16.
- [56] M.Z. Bazant, M.S. Kilic, B.D. Storey, A. Ajdari, *Advances in Colloid and Interface Science* 152 (1–2) (2009) 48–88.
- [57] M.S. Kilic, M.Z. Bazant, A. Ajdari, *Physical Review E* 75 (2) (2007) 1–11.
- [58] J. Lyklema, *Fundamentals of Interface and Colloid Science*, in: *Solid–liquid Interfaces*, vol. II, Academic Press, San Diego, CA, 2001.
- [59] E.M. Itskovich, A.A. Kornyshev, M.A. Vorotyntsev, *Physica Status Solidi A* 39 (1) (1977) 229–238.
- [60] A.A. Kornyshev, M.A. Vorotyntsev, *Electrochimica Acta* 26 (3) (1981) 303–323.
- [61] Ajdari, *Physical Review E* 61 (1) (2000) 45–48.
- [62] Bonnefont, F. Argoul, M.Z. Bazant, *Journal of Electroanalytical Chemistry* 500 (1–2) (2001) 52–61.
- [63] L.H. Olesen, H. Bruus, A. Ajdari, No. 056313, *Physical Review E* 73 (5) (2006) 1–16.
- [64] P.M. Biesheuvel, M. van Soestbergen, M.Z. Bazant, *Electrochimica Acta* 54 (21) (2009) 4857–4871.
- [65] P.M. Biesheuvel, A.A. Franco, M.Z. Bazant, *Journal of the Electrochemical Society* 156 (2) (2009) 225–233.
- [66] P.M. Biesheuvel, Y. Fu, M.Z. Bazant, *Physical Review E* 83 (6) (2011) 1–17.
- [67] D.R. Lide (Ed.), *CRC Handbook of Chemistry and Physics*, ninetieth ed., CRC Press/Taylor & Francis, Boca Raton, FL, 2010.
- [68] J.N. Israelachvili, *Intermolecular and Surface Forces*, third ed., Academic Press, San Diego, CA, 2010.
- [69] S. Senapati, A. Chandra, *Journal of Physical Chemistry B* 105 (22) (2001) 5106–5109.
- [70] J. Dzubiella, J.P. Hansen, No. 234706, *Journal of Chemical Physics* 122 (23) (2005) 1–14.
- [71] G.J. Janz, R.P.T. Tomkins, *Nonaqueous Electrolytes Handbook*, vol. I, Academic Press, New York, NY, 1972.
- [72] G. Moumouzias, G. Ritzoulis, *Journal of Chemical & Engineering Data* 42 (4) (1997) 710–713.
- [73] J. Chmiola, G. Yushin, Y. Gogotsi, C. Portet, P. Simon, P.L. Taberna, *Science* 313 (5794) (2006) 1760–1763.
- [74] Y.-J. Kim, Y. Masutawa, S. Ozaki, M. Endo, M.S. Dresselhaus, *Journal of the Electrochemical Society* 151 (6) (2004) 199–205.
- [75] M. Yang, Y.J. Kim, M. Endo, H. Kanoh, M. Yudasaka, S. Iijima, K. Kaneko, *Journal of the American Chemical Society* 129 (1) (2007) 20–21.
- [76] R. Halliday, Resnick, J. Walker, *Fundamentals of Physics*, ninth ed., John Wiley & Sons, Hoboken, NJ, 2010.
- [77] J. Griffiths, *Introduction to Electrodynamics*, third ed., Prentice Hall, Upper Saddle River, NJ, 1999.
- [78] Y. Marcus, *Chemical Reviews* 88 (8) (1988) 1475–1498.
- [79] M. Noked, E. Avraham, A. Soffer, D. Aurbach, *Journal of Physical Chemistry C* 114 (31) (2010) 13354–13361.
- [80] V.N. Afanasev, A.N. Ustinov, *Electrochimica Acta* 54 (26) (2009) 6455–6463.
- [81] N. Nanbu, T. Ebina, H. Uno, S. Ishizawa, Y. Sasaki, *Electrochimica Acta* 52 (4) (2006) 1763–1770.
- [82] O. Ania, J. Pernak, F. Stefaniak, E. Raymundo-Piñero, F. Béguin, *Carbon* 47 (14) (2009) 3158–3166.
- [83] L. Yang, B.H. Fishbine, A. Migliori, L.R. Pratt, *Journal of the American Chemical Society* 131 (34) (2009) 12373–12376.
- [84] B. Merlet, P.A. Rotenberg, P.-L. Madden, P. Taberna, Y. Simon, Gogotsi, M. Salanne, *Nature Materials* 11 (4) (2012) 306–310.